Design and Initial Testing of An Integrated Switched Reluctance Starter/Generator System for Unmanned Aerial Vehicle

Erxin Zhao, Shoujun Song, *Senior Member, CES and IEEE,*
Zhen Ma, Xueping Zhang, Le Ning, Yang Liu

***Abstract*—According to specific performance requirements, an integrated switched reluctance starter/generator system, which can start the engine and supply electrical energy to the loads, is designed and manufactured for the unmanned aerial vehicle. Considering the required starting torque and speed range, the geometrical dimensions of the switched reluctance machine are calculated based on the output equation and further optimized with finite element analysis, and the flux-linkage, inductance and static torque characteristics are illustrated. To verify the performances of the designed system, detailed simulation with the model considering piston engine and experiment using the test bench are carried out.**

***Index Terms*—Integrated starter/generator system, switched reluctance machine (SRM), unmanned aerial vehicle (UAV).**

I. Introduction

SOME big unmanned aerial vehicles (UAVs) are propelled by piston engines [1]. The engine needs to be started first, and then it operates as a prime mover and drives a generator to supply electrical energy. In traditional UAVs, a specific motor is used to start the engine, and a generator is adopted to produce electrical energy, which means the starting and generating function are separated. This type of arrangement makes the system complex, and increases the size and weight, which is undesired for aviation applications [2].

The main motors suitable for the integrated starter/generator (ISG) system are permanent magnet machines and switched reluctance machines [3][4]. Permanent magnet starter/generator (PMSG) has advantages like high power density and energy conversion efficiency [5][6]. However, because the flux of the permanent magnets cannot be adjusted, the flexibility and stability of the PMSG under both starting and generating modes should be further improved.

Switched reluctance machine (SRM) is an attractive candidate for the ISG system due to its simple structure, high reliability, wide speed range, low maintenance requirement and so on [7][8]. It can be used as a motor or a generator. When it works as the motor, the torque current ratio is high. When it works as the generator, the output power and the output voltage can be adjusted under different working conditions. It can also work in fault state when a phase defaults [9]. In [10], a high speed switched reluctance starter/generator system was implemented. The simulation model was constructed, and the control parameters were optimized. In [11][12], a shaft line-embedded switched reluctance starter/generator for an aircraft gas turbine was presented, which needs to run in an ambient temperature of around 350°C, and at the same time has a very high specific output. In [13], a fast analytical modeling method for an integrated switched reluctance starter/generator was proposed based on the Fourier series. In [14], a sliding mode variable structure controller was designed to build and adjust the output voltage of the switched reluctance starter/generator in the switch over process. In [15], the fault-tolerant performances of the dual-channel switched reluctance starter/generator and the dual-channel doubly salient permanent magnet starter/generator were compared, and the results show that the former has more stable performances.

In this paper, the integrated switched reluctance starter/generator (SRSG) system for UAV is presented. The structure and size of the machine are determined based on the starting torque and speed range. Thereafter, the flux linkage, inductance and torque characteristics are obtained by static magnetic field analysis with the 2D FEA model. The starting and generating performances of the system are evaluated by simulation. Furthermore, the starting performances of the system are verified by experiment as well. The main contribution of this paper is design and testing of the SRSG system considering the special resistance torque characteristics of the piston engine.

The paper is organized as follows. In Section II, the design process and preliminary evaluation of the SRSG system are described in detail. The modeling and simulation of the system are illustrated in Section III. In Section IV, the experiments and analysis are carried out. Section V concludes this paper.

II. Design and Preliminary Evaluation

The schematic diagram of the integrated starter/generator is shown in Fig. 1. The SRSG is coaxially connected to the piston engine. SRSG works in motoring mode and drives the engine and propeller when the starting phase controller receives the start command. It will stop working after the engine running at idle state. Then the SRSG will switch to generating mode when

Manuscript was submitted for review on 01, October, 2018
This work was supported by the Key Research and Development Plan of Shaanxi Province under Grant 2018GY-185, Xi'an Science and Technology Plan under Grant 2017086CG/RC049(XBGY002), the ASN Innovation Development Fund under Grant ASN-IF2015-3110, and the Fundamental Research Funds for the Central Universities under Grants 3102017AX007.
E. Zhao and S. Song are with Northwestern Polytechnical University, Xi'an 710072, China (e-mail: sunnyway@nwpu.edu.cn).
Z. Ma, X. Zhang, L. Ning and Y. Liu are with Xi'an ASN Technology, Xi'an 710065, China.
Digital Object Identifier 10.30941/CESTEMS.2018.00048

the system speeds up to the required minimum speed.

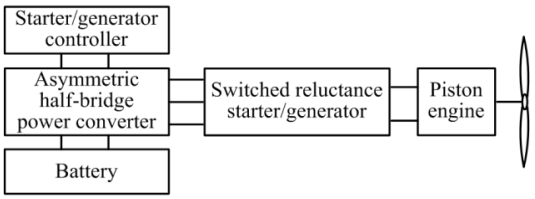

Fig. 1. Schematic diagram of the integrated starter/generator system.

A. Electromagnetic design

The empirical formulas are applied in electromagnetic design process based on design objects. Main structural parameters are calculated and verified by finite element calculation of electromagnetic field.

The technical requirements of the considered SRSG system are as follows:

Rated power	2kW
Rated voltage	60VDC
Rated speed	4800rpm
Rated efficiency	≮80%
Starting torque	≮15Nm
Ignition speed	700rpm
Disconnection speed	1000rpm
Weight of the SRM	≯6kg

To reduce the ripple of the torque and voltage, 4-phase 16/12-pole topology is selected. The output equation of SRM expressed by torque is

$$T = kD_r^2 L_{stk} \tag{1}$$

where T is the required lowest starting torque, which is 15Nm in this paper. k is the torque coefficient, D_r is the rotor outer diameter, and L_{stk} is the core length of SRM. The value of k is proportional to the product of electrical and magnetic load. For aviation applications, its value range is 20.7 -51.7 kNm/m^3.

The ratio of the core length to the rotor diameter is defined as

$$\lambda = \frac{L_{stk}}{D_r} \tag{2}$$

The range of λ is generally 0.5-3. After determining T and λ, L_{stk} and D_r can be calculated by (2).

In order to obtain larger output power and reduce the volt-ampere capacity requirement of the power converter, the air gap length g should be shortened as far as possible. However, due to the limitation of processing and assembly technique, as well as the consideration of reliable operation, g should not be too short. The air gap length g of small motor is no shorter than 0.25mm.

Stator pole width t_s and rotor pole width t_r can be calculated using

$$t_s = 2\left(r_1 + g\right)\sin\frac{\beta_s}{2} \tag{3}$$

$$t_r = 2r_1 \sin\frac{\beta_r}{2} \tag{4}$$

where r_1 is the radius of the rotor, β_s and β_r are the stator and rotor pole arcs, respectively.

In order to ensure that the maximum magnetic density of the yoke is not oversaturated, the yoke height of stator y_s and rotor y_r are determined by

$$y_s = \left(1.2 \sim 1.4\right)\frac{t_s}{2} \tag{5}$$

$$y_r = \left(1.2 \sim 1.4\right)\frac{t_r}{2} \tag{6}$$

The shaft diameter D_{sh} of the motor should not be very small, otherwise it will affect the mechanical strength, as well as causing rotor vibration and eccentricity which would increase the motor noise. At the same time, it should not be too big. The appropriate shaft diameter should be chosen to provide a large second air gap and a high rotor yoke. It can be generally selected as

$$D_{sh} = \left(0.4 \sim 0.5\right)D_r \tag{7}$$

Series winding numbers of each phase can be calculated by

$$N_{ph} = \frac{30}{\pi^2}\frac{N_r U \theta_c}{B_{\delta} D_r L_{stk}} \tag{8}$$

Based on the above design process, the main parameters of the SRM are obtained and shown in Table I. It should be noted that the final determination of the parameters not only depends on the above equations, but also on other considerations, such as the operating condition, manufacture complexity and external connection constraint. For example, in this paper, y_s and y_r are larger than the calculating results to reduce the saturation, and the shaft diameter is limited by the external mechanical connection.

TABLE I
MAIN PARAMETERS OF THE SRM

Parameter	Value
Phase number	4
Stator pole number N_s	16
Rotor pole number N_r	12
Stator outer diameter D_s	150mm
Rotor outer diameter D_r	90mm
Core length L_{stk}	45mm
Air gap length g	0.5mm
Stator pole arc β_s	10.5°
Rotor pole arc β_r	11.5°
Stator pole width t_s	8.3 mm
Rotor pole width t_r	9.1 mm
Stator yoke y_s	6 mm
Rotor yoke y_r	8 mm
Shaft diameter D_{sh}	25 mm
Series winding numbers N_{ph}	20
Number of parallel conductors	8
Coil space factor	57%
Weight	4.5kg

The cross-sectional view of the stator and rotor are shown in Fig. 2.

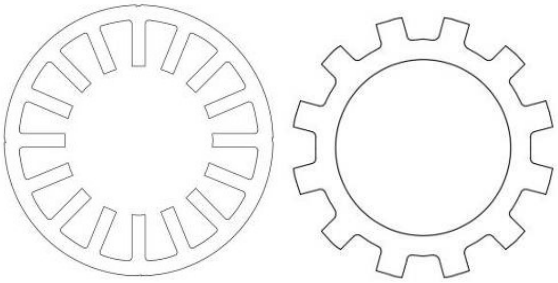

(a) Stator (b) Rotor

Fig. 2. Cross-sectional view of the stator and rotor.

B. Preliminary Evaluation

1) Static characteristic analysis

The magnetic field distribution, flux linkage ψ, inductance L and torque T of the designed SRM can be analyzed and calculated with FEM. Thereafter, the static characteristics of the machine can be obtained, which is crucial to performance verification.

Fig. 3 presents the relationship between flux linkage and current under different rotor positions.

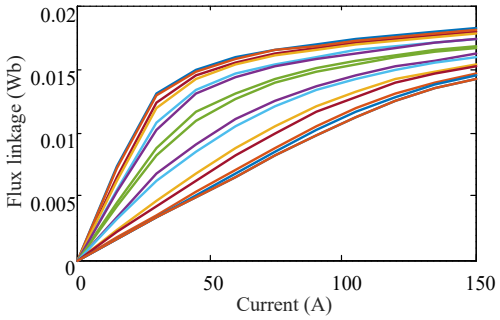

Fig. 3. Flux-linkage characteristics.

As shown in Fig. 3, the rotor gradually moves from the minimum inductance position to the maximum inductance position. The flux linkage first increases fast, which is easier to reach saturation. Then it grows slow, and the nonlinear relationship between flux linkage and current starts to present.

Fig. 4 presents the relationship between inductance and rotor position with certain phase current.

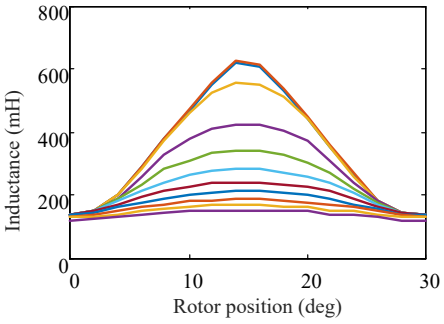

Fig. 4. Inductance characteristics.

Fig. 5 presents the relationship between static torque and rotor position with certain phase current, where 0° and 15° are the unaligned and aligned rotor position, respectively.

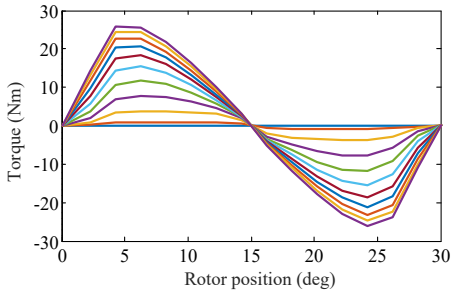

Fig. 5. Static torque characteristics

In static magnetic field analysis, single phase excitation is performed to observe the magnetic field distribution when SRM is located in the unaligned and partial aligned position as shown in Fig. 6.

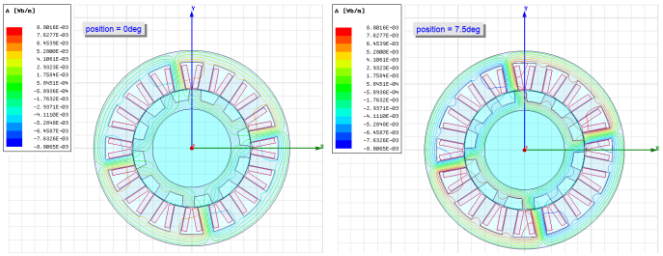

Fig. 6. Magnetic field distribution of single phase excitation.

2) Motoring performance analysis

Fig. 7 shows the phase current and torque under motoring mode obtained by finite element analysis in Maxwell. The speed is 700 rpm, and the current chopping range is 140-160A. The turn-on and turn-off angles are 0◦ and 15◦, respectively.

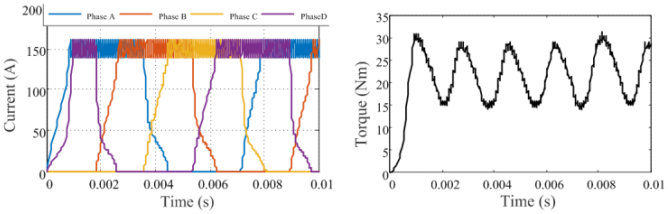

Fig. 7. Phase current and torque under motoring mode.

3) Generating performance analysis

Fig. 8 shows the phase current, torque and voltage under generating mode. The speed is 4800 rpm, and the turn-on and turn-off angles are 12° and 24°, respectively.

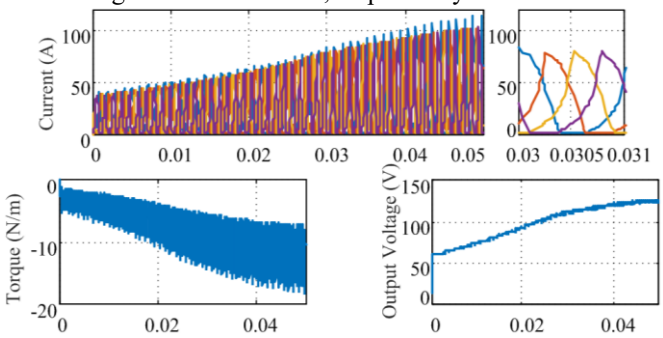

Fig. 8. Phase current, torque and voltage under generating mode.

III. System Modeling and Simulation

A. Dynamic model of engine starting process

During starting, the resisting force mainly include compression resistance of cylinder, frictional resistance of assembly parts, inertia force of rotating parts and so on. The resisting forces act on the crankshaft and produce corresponding resistance torque.

1) Compression resistance torque of cylinder

The air inside the cylinder acts directly on the top of the piston and push the piston back and forth. The compressed air works negatively when the piston is in the compression state. The compressed air works positively when the piston is in the expansion state. As shown in Fig. 9, when the engine is starting, the gas pressure inside the cylinder P_g transfers to the crankshaft through the piston. P_k is the force along the direction of connecting rod which can be decomposed into tangential

force P_T and radial force P_r. P_T and P_r are expressed as

$$P_k = \frac{P_g}{\cos\beta} \tag{9}$$

$$P_T = P_k \sin(\alpha+\beta) = \frac{P_g \sin(\alpha+\beta)}{\cos\beta} \tag{10}$$

where α is the crank angle, β is the swinging angle of the connecting rod.

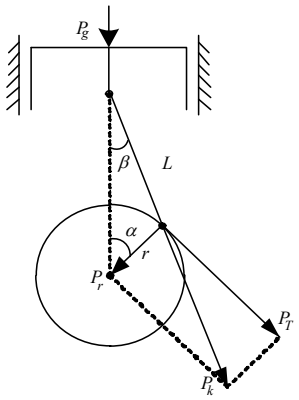

Fig. 9. Force diagram of crank-link mechanism

The gas compression process is similar to the gas state equation, which is

$$P_0 V_0^{n1} = P_g V_g^{n1} \tag{11}$$

where P_0 is the atmospheric pressure, V_0 is the cylinder working volume at the beginning of the compression process, n_1 is the adiabatic coefficient, V_g is the cylinder working volume when the crankshaft turning.

The initial compression resistance torque is derived as

$$T_C = P_T r = \frac{P_0 V_0^{n1} \sin(\alpha+\beta)}{\left\{V_c + \left[r(1-\cos\alpha)+\lambda r(1-\cos 2\alpha)/4\right]\pi(D/2)^2\right\}^{n1}\cos\beta}\pi\left(\frac{D}{2}\right)^2 r \tag{12}$$

where V_C is the combustion chamber space, s is the piston displacement, λ is the crank radius ratio.

2) Frictional resistance torque

The frictional resistance torque is demonstrated as

$$T_f = \frac{N_f}{2\pi n_{st}} = 3.18 P_f V_h i\tau + k\omega \tag{13}$$

where V_h is the working volume of engine horizontal bar, i is the number of engine cylinders, τ is the number of engine work cycles, P_f is the average pressure of starting frictional resistance, k is the load factor, and ω is the angular velocity of the crankshaft.

P_f is determined according to the following empirical equation.

$$P_f = 38.4\times10^5 \times \gamma^{0.25} \tag{14}$$

where γ is the viscosity of the lubricating oil at the starting temperature.

3) Inertial resistance torque

The inertial resistance torque can be expressed as

$$T_I = T_e - T_f - T_C = J\frac{d\omega}{dt} \tag{15}$$

where T_e is the electromagnetic torque.

B. Simulation

1) Starting stage

Fig. 10 shows the torque and speed response at starting stage obtained by dynamic simulation in Matlab. In the figure, 1/3 cycle and 1/2 cycle indicate the conduction angle. For 1/3 cycle conduction, the turn-on and turn-off angles are 0° and 10°, respectively. The conduction angle is 10°, and is 1/3 of the inductance period of the considered SRM, which is 30°. For 1/2 cycle conduction, the turn-on and turn-off angles are 0° and 15°, respectively. The conduction angle is 10°, and is 1/2 of the inductance period.

From the simulation results, it can be seen that in the low-speed zone, under the condition of fixed turn-on and turn-off angles, the output torque is no less than 20Nm, which meets the requirement of design. When speed reaches about 700 rpm, it declines more slowly at 1/2 cycle mode, which results in larger negative torque. Therefore, the angle position control (APC) should be adopted to optimize the turn-on and turn-off angles according to the efficiency.

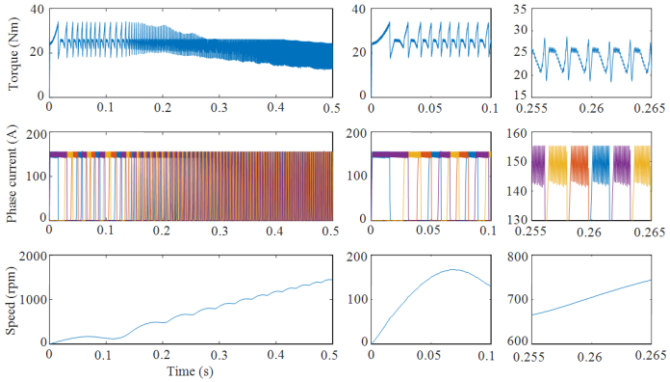

(a) 150A, 1/3 cycle conduction.

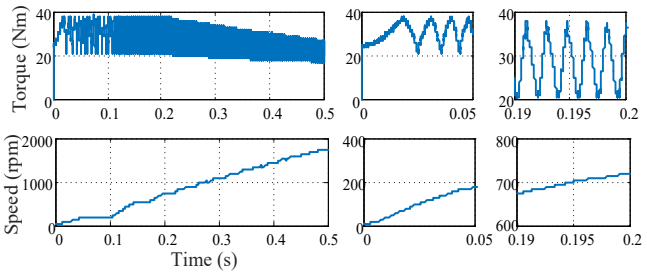

(b) 150A, 1/2 cycle conduction.

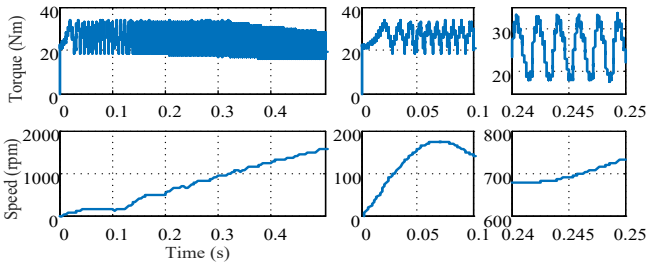

(c) 120A, 1/2 cycle conduction.

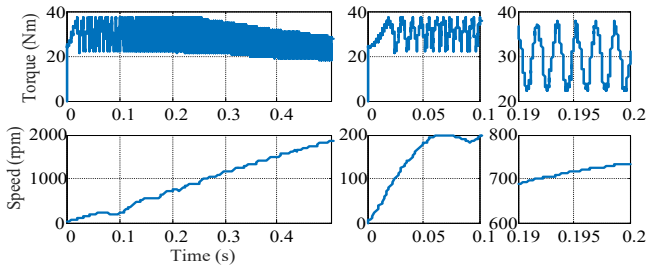

(d) conduction in advance

Fig. 10. Torque and speed response at starting stage.

2) Power generation stage

Fig. 11 shows the torque, output voltage and current at power generation stage. The speed is 4800rpm, the maximum excitation current is 80A, the output voltage is 60V and the

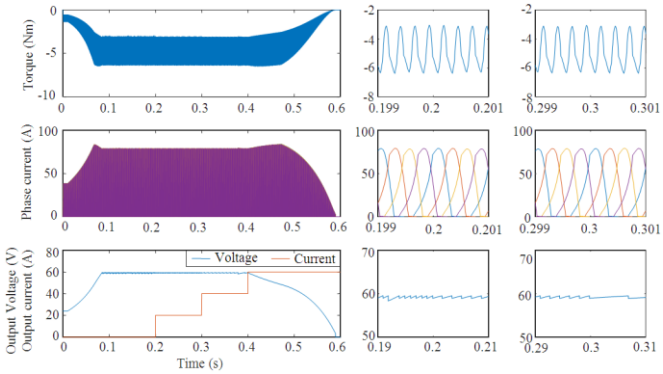

(a) Output voltage: 60V

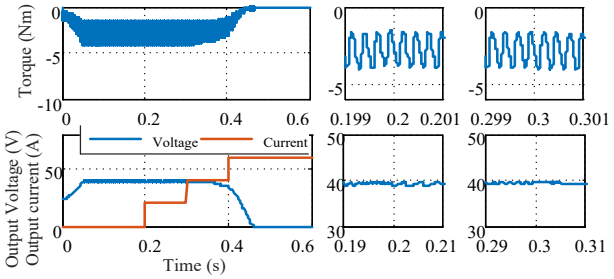

(b) Output voltage:40V

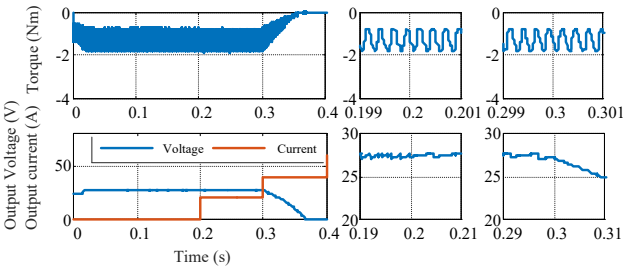

(c) Output voltage: 28V

Fig. 11. Torque, output voltage and current at power generation stage.

IV. Experimental Verification and Analysis

A. Hardware design

Fig. 12 shows the overall scheme of the SRM drive system. Asymmetric half-bridge topology is selected for the converter, and the control algorithm is implemented with DSP TMS320F28335 and FPGA EP2C8Q208C8. The phase current and rotor position signals are processed by A/D converter and rotary transformer decoder AD2S1210, respectively, and then input into FPGA. The real-time rotor position is compared with the turn-on and turn-off angels to get the APC control signals, and the real-time phase current is compared with the current chopping range to get the current chopping signals. The logic synthesis of the APC and current chopping signals is carried out in FPGA to get the control signal. To adjust the speed at the starting stage and voltage at the generating stage as required, the closed-loop control methods, such as PI control, are implemented in DSP. The communication between computer and DSP is RS232, and the user can get system operation information and input control requirements with the computer.

B. SRM prototype and loading platform

Fig. 13 shows the photos of the SRM prototype and the loading platform, respectively.

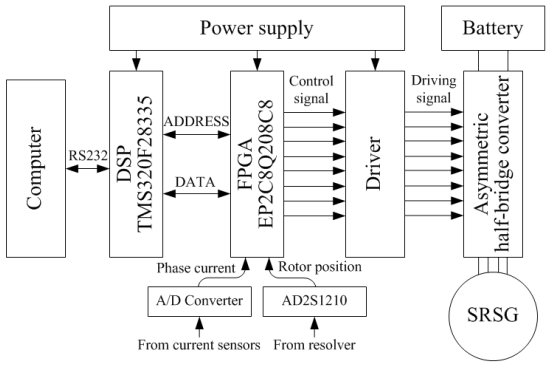

Fig. 12. Overall scheme of the SRM drive system

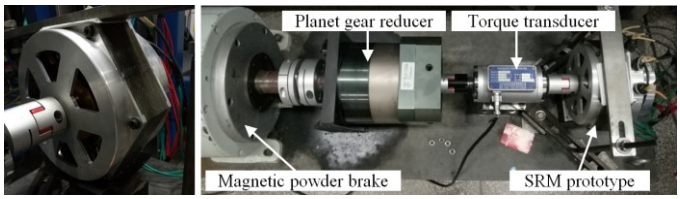

Fig. 13. SRM prototype and the loading platform

C. Experimental results and analysis

Fig. 14 shows the experimental results. The battery voltage is 57.5V, the turn-on and turn-off angles are 0° and 10°, respectively. The current of the magnetic powder brake is 0.5A, which corresponds to 16Nm loading torque.

As shown in Fig. 14(a), at the beginning of starting stage, current rises fast due to the low back EMF. The voltage is taken down to about 48V. Thereafter, the current reaches to the chopping state. During the low speed stage, the back EMF is low. Therefore, the current goes up fast, which can reach to about 100A. The speed rises fast because the produced electromagnetic torque is large. As the speed increases, the back EMF rises, therefore the current increases slowly and the electromagnetic torque decreases. Finally the speed rises slowly and tends to be steady. It can be seen that speed reaches to 750rpm after 0.45s, which means that the output torque is no lower than 16Nm at 0~700rpm and meet the design requirements. As shown in Fig.14 (b), the system tends to be steady after 0.3s, which means that the starting time can be shorten by increasing current chopping level. In Fig. 14, the

magnitude and hysteresis width of each phase current are not identical due to the inaccuracy of the current sensors, which will be improved in the future work.

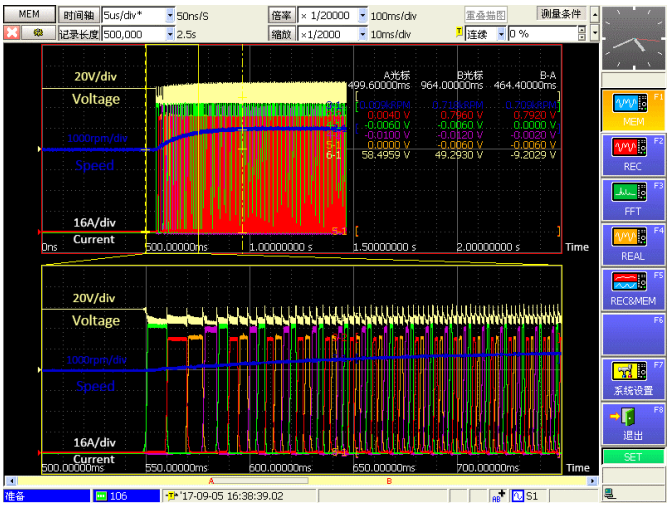

(a) Current chopping level:100A

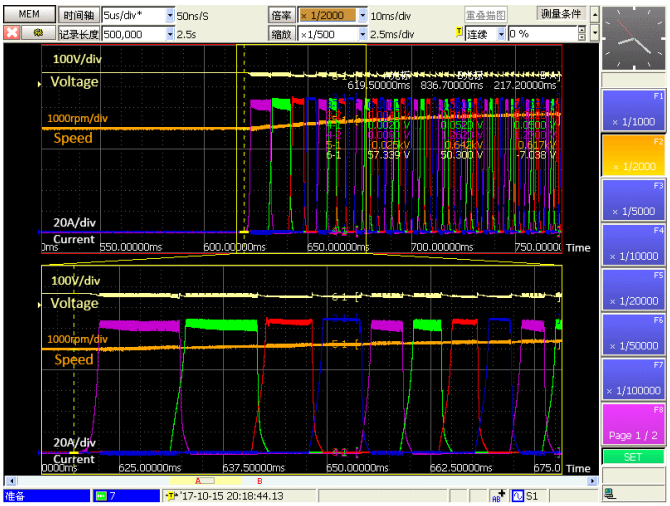

(b) Current chopping level:120A

Fig. 14. Experimental results.

V. Conclusion

In this paper, considering the outstanding performance merits of the switched reluctance machine, an integrated starter/generator system is presented for UAV, which can accomplish the starting and generating function with a single SRM. The design process of the SRM is described in detail, and the flux-linkage, inductance and static torque characteristics of the design scheme are analyzed by the finite element method. The model of the switched reluctance starter/generator system considering the resisting torque of the piston engine is built in Matlab, and the starting and generating modes are simulated under different operating conditions. Furthermore, with the specialized test bench, the starting capability of the SRM prototype is evaluated by experiments. Both the simulation and experimental results indicate that the performances of the designed SRSG system meet the technical requirements. Further test, analysis and improvement will be carried out in the near future.

References

[1] Z. Pan, Q. He, X. Zhang, and D. Zhang, "Numerical simulation of 2-stroke diesel engine for light aircraft," IEEE Aerospace and Electronic Systems Magazine, vol. 30, no. 3, pp. 4-10, 2015.

[2] B. S. Bhangu and K. Rajashekara, "Electric starter generators: their integration into gas turbine engines," IEEE Industry Applications Magazine, vol. 20, no. 2, pp. 14-22, 2014.

[3] R. Bojoi, A. Cavagnino, M. Cossale, and A. Tenconi, "Multiphase starter generator for a 48-V mini-hybrid powertrain: design and testing," IEEE Transactions on Industry Applications, vol. 52, no. 2, pp. 1750-1758, 2016.

[4] M. D. Bui, S. Schneider, S. Arnaout, and U. Schaefer, "Torque maximization of a high-speed switched reluctance starter in acceleration test," European Conference on Power Electronics and Applications (EPE), pp. 1-11, 2013.

[5] L. Chedot, G. Friedrich, J. M. Biedinger, and P. Macret, "Integrated starter generator: the need for an optimal design and control approach. application to a permanent magnet machine," IEEE Transactions on Industry Applications, vol. 43, no. 2, pp. 551-559, 2007.

[6] K. T. Chau, C. Chan, and C. Liu, "Overview of permanent-magnet brushless drives for electric and hybrid electric vehicles," IEEE Transactions on Industrial Electronics, vol. 55, no. 6, pp. 2246-2257, 2008.

[7] B. Burkhart, A. Klein-Hessling, I. Ralev, C. P. Weiss, and Rik W. De Doncker, "Technology, research and applications of switched reluctance drives," CPSS Transactions on Power Electronics and Applications, vol. 2, no. 1, pp. 12-27, 2017.

[8] P. J. dos S. Neto, T. A. dos S. Barros, M. V. de Paula, R. R. de Souza, and E. R. Filho, "Design of computational experiment for performance optimization of a switched reluctance generator in wind systems," IEEE Transactions on Energy Conversion, vol. 33, no. 1, pp. 406-419, 2018.

[9] J. F. Marques, J. O. Estima, N. S. Gameiro, and A. J. M. Cardoso, "A new diagnostic technique for real-time diagnosis of power converter faults in switched reluctance motor drives," IEEE Transactions on Industry Applications, vol. 50, no. 3, pp. 1854-1860, 2014.

[10] J. Sun, Z. Kuang, H. Wu, S. Wang, and G. Ning, "Implementation of a high-speed switched reluctance starter/generator system," International Conference on Electrical Machines and Systems, pp. 1-5, 2011.

[11] D. J. Powell, G. W. Jewell, S. D. Calverley, and D. Howe, "Iron loss in a modular rotor switched reluctance machine for the "more-electric" aero-engine," IEEE Transactions on Magnetics, vol. 41, no. 10, pp. 3934-3936, 2005.

[12] R. Hall, A. G. Jack, B. C. Mecrow, and A. J. Mitcham, "Design and initial testing of an outer rotating segmented rotor switched reluctance machine for an aero-engine shaft-line-embedded starter/generator," IEEE International Conference on Electric Machines and Drives, pp. 1870-1877, 2005.

[13] W. Ding and D. Liang, "A fast analytical model for an integrated switched reluctance starter/generator," IEEE Transactions on Energy Conversion, vol. 25, no. 4, pp. 948-956, 2010.

[14] Y. Liu, Z. Zhou, J. Song, B. Fan, and C. Wang, "Based on sliding mode variable structure of studying control for status switching of switched reluctance starter/generator," Chinese Automation Congress, pp. 934-939, 2015.

[15] Q. Ze, P. Kou, D. Liang, and Z. Liang, "Fault-tolerant performances of switched reluctance machine and doubly salient permanent magnet machine in starter/generator system," International Conference on Electrical Machines and Systems, pp. 3417-3423, 2014.

Erxin Zhao received the B.S. degree in electrical engineering from Northwestern Polytechnical University, Xi'an, China, in 2015, where he is currently working toward the M.S. degree in electrical engineering.

His research interests include design and control of switched reluctance machine.

Shoujun Song (M'08-SM'16) received the B.S. and M.S. degrees from Northwestern Polytechnical University, Xi'an, China, in 2003 and 2006, respectively, and the Dr.-Ing. degree from the Technical University of Berlin, Berlin, Germany, in 2009, all in electrical engineering.

He is currently an Associate Professor with the College of Automation, Northwestern Polytechnical University. His research interests include electric machines and drives with emphasis on switched reluctance machine design and control.